

# Image analysis for discrimination of cervical neoplasia

## Brian W. Pogue

Thayer School of Engineering  
Dartmouth College  
Hanover, NH 03755

## Mary-Ann Mycek

Department of Physics and Astronomy  
Dartmouth College  
Hanover, NH 03755

## Diane Harper

Department of Community and Family Medicine  
Dartmouth-Hitchcock Medical Center  
Lebanon, NH 03756

**Abstract.** Colposcopy involves visual imaging of the cervix for patients who have exhibited some prior indication of abnormality, and the major goals are to visually inspect for any malignancies and to guide biopsy sampling. Currently colposcopy equipment is being upgraded in many health care centers to incorporate digital image acquisition and archiving. These permanent images can be analyzed for characteristic features and color patterns which may enhance the specificity and objectivity of the routine exam. In this study a series of images from patients with biopsy confirmed cervical intraepithelial neoplasia stage 2/3 are compared with images from patients with biopsy confirmed immature squamous metaplasia, with the goal of determining optimal criteria for automated discrimination between them. All images were separated into their red, green, and blue channels, and comparisons were made between relative intensity, intensity variation, spatial frequencies, fractal dimension, and Euler number. This study indicates that computer-based processing of cervical images can provide some discrimination of the type of tissue features which are important for clinical evaluation, with the Euler number being the most clinically useful feature to discriminate metaplasia from neoplasia. Also there was a strong indication that morphology observed in the blue channel of the image provided more information about epithelial cell changes. Further research in this field can lead to advances in computer-aided diagnosis as well as the potential for online image enhancement in digital colposcopy. © 2000 Society of Photo-Optical Instrumentation Engineers. [S1083-3668(00)00401-9]

Keywords: image analysis; colposcopy; biopsy; computer-aided diagnosis.

Paper JBO-90017 received March 17, 1999; revised manuscript received Aug. 13, 1999; accepted for publication Aug. 24, 1999.

## 1 Introduction

Colposcopy was developed in 1925 by Hinselmann to direct the cervical biopsy placement to improve the correlation between cervical cytology and histology.<sup>1</sup> The transformation zone of the cervix could be colposcopically identified after 5% acetic acid was applied to the cervix. Areas of abnormality are defined colposcopically by: (i) the degree of whitening after acetic acid solution application, (ii) the roughness of the surface contour, (iii) the margins of the lesions, and (iv) the vascular pattern and intercapillary distance. The correlation between cytology and histology improved with colposcopically directed biopsies from less than 50% to almost 90% when the entire transformation zone was visible in expert hands. When the squamocolumnar junction could not be seen, the colposcopically directed biopsy was not much better than cytology alone at a 60% correlation.<sup>2</sup>

There is agreement among colposcopists that, in general, expert correlation between the colposcopic image and the specimen histology ranges from 50% to 75%. This considers cross agreements between all tissue types: normal, metaplastic, all stages of cervical intraepithelial neoplasia (CIN 2/3), and cancer.<sup>3,4</sup> Yet, in inexperienced hands, the colposcopic impression correlates to the histologic specimen less than 35% of the time, with the most difficulty encountered in dif-

ferentiating benign epithelial changes from CIN 2/3.<sup>5</sup>

Digital imaging in colposcopy has facilitated the development of archival records for many clinical purposes: auditing of cytology, colposcopy and histology correlations, quality assurance of care, and monitoring disease regression and progression with simple planar measurement tools.<sup>6–9</sup> Although the advance in digital imaging has been employed mainly for image archiving of patient records, the digitized colposcopic images contain two important types of diagnostic information: tissue structure and color. Structural information appears as morphological features reflecting underlying tissue architecture, while color content, which is affected by tissue optical absorption and scattering, reflects tissue biochemistry and substructure. Although this information could be quantified and enhanced via standard image processing techniques, in conventional use these images remain unprocessed. Thus, disease diagnoses are made off-line from pathological examinations of biopsied tissue samples obtained during colposcopy. Digital imaging colposcopy now allows the colposcopist to take advantage of the mature field of image analysis and processing, where image features, color patterns, and trends can be reliably detected and quantified.

Semiautomated image processing tools can be incorporated into a computer coupled colposcope to aid the physician, once the appropriate metrics have been determined to quantify

the important morphologic features. An example of this is the the development of neural network algorithms using intercapillary distance, lesion area, and perimeter to aid the less experienced colposcopist in determining the most diseased cervical lesion for biopsy.<sup>10</sup> This type of processing may be especially useful in problematic diagnoses, where an objective number can be assigned to the color or structural changes seen in the cervical tissue. While image analysis of the entire field is possible, it is more illustrative and potentially useful to perform analyses on regions of interest (ROI) that have been defined within an image by the clinician. In this way, the analysis is confined to that region as defined by the user, and takes advantage of the knowledge of the user. If this approach is not used, then the analysis is blind and must be able to deal with a larger range of problems such as intensity variation across the image or depth of focus variations. The first stage in such a development is to determine and test the most useful measures to analyze and quantify regions of cervical tissue, within specified regions of interest.

In this study, three tissue types in particular have been examined including mature squamous epithelium (MSE), immature squamous metaplasia (ISM), and cervical intraepithelial neoplasia grade 2/3 (CIN 2/3). The goal of the study was to take a sample of representative tissue images, and determine some simple metrics which would be capable of discriminating between them based upon the information from the colposcope color image. To this end, we examined the color information in the red, green and blue (RGB) pixel intensities and intensity variations, as well as some simple texture detecting features including spatial frequency analysis, fractal dimension, and Euler number. These analyses are the first steps in designing a computer-aided colposcopy workstation that can serve as a useful tool and guide for the practicing colposcopist. Additionally, the analysis of typical cervical tissue features including multiple optical wavelengths and multiple spatial frequencies may potentially lead to an improved understanding of the morphology of cervical tissue lesions.

## 2 Methods

### 2.1 Patients

Women between the ages of 18 and 65 were recruited for this study if they had been referred to colposcopy. Referral to colposcopy was based on abnormal cytology, [two consecutive Pap tests showing atypical squamous cells of undetermined significance (ASCUS), or one Pap test showing atypical glandular cells of undetermined significance (AGUS), low grade squamous intraepithelial lesion (LSIL), high grade squamous intraepithelial lesion (HSIL) or squamous cancer] or an abnormal visual exam at routine screening. All women underwent the standard colposcopic procedure. The cervix was visualized and 5% acetic acid was applied continuously for three to four minutes to the surface, allowing adequate time for the most dense acetowhite lesions to appear. The squamocolumnar junction and the transformation zone were identified; and then the abnormal lesions were analyzed. The first image was captured at a 4× magnification giving a panoramic view of the entire cervical field at maximal acetowhitening. Subsequent images were taken at 10× and 16× of the area of most concern focusing either on margins or vasculature patterns that are most easily seen at higher powers. Ace-

**Table 1** Details of biopsy pathology results from the nine abnormal colposcopy patients in this study. These same specimens correspond to specimen numbers 1–9 in Figures 2–5.

Specimen	Pathologic diagnosis
1	Focal adenocarcinoma in situ
2	CIN II
3	CIN II/III
4	CIN II/III
5	CIN II/III
6	CIN II/III
7	CIN II/III
8	CIN III
9	CIN III

tic acid was reapplied to the cervix when the transient acetowhitening started to fade. The images in this study were all taken between 1 and 3 min after application of acetic acid, to provide a uniform whitening affect across all the images. Color filter images were taken when contrasting images were visible, but generally the green filter darkened the digital image so much that the details of the lesion were obscured. Lugol's solution was applied to the cervix after all acetic acid images were taken. This iodine based solution stained the mature cervical squamous epithelium mahogany brown, and the immature or neoplastic epithelium a mustard yellow or variegated pattern. Lugol's is used clinically to distinguish the borders of a lesion clearly from the normal mature cervical epithelium, as it obscures whitening and vessel patterns. A panoramic colposcopic image was taken at 4× with Lugol staining, however these images were not used in this study as we believed the acetowhitened images to be more useful for the current analysis.

Images were interpreted after all patient images were taken and biopsy confirmation had been received for suspicious sites. For this study, nine patients with biopsy confirmed neoplasia were included in the study, with biopsy results included in Table 1.

### 2.2 Colposcope

The colposcope is a Carl Zeiss 1-FC system ZMS-506-II with magnifications of 4×, 6×, 10×, 16×, and 25× illuminated by a fiberoptic 12 V/100 W halogen light with 20× eye binoculars. A DAGE-MTI DC-330 three channel charge-coupled device color video camera, automatically white balanced, was mounted to the colposcope allowing real-time video display of the examination. Although this video system is not commonly used in Colposcopy Clinics because of its cost, the parts to assemble it were standard. Images were captured by an integrated video frame grabber and video display card using the RGB video signal at 24 bit resolution. ColpoShot is the custom-designed software copyrighted by TeleComputing Solutions, Inc. (Hanover, NH) which integrates the unique

image into the patient's medical record. Unlimited images can be taken of any one patient. The images are stored in (JPEG) format with minimal compression.

### 2.3 Region of Interest Analysis

All digital images were stored as JPEG files on the computer typically at  $640 \times 480$  pixel dimensions, with 16 million colors. Images were loaded into Adobe Photoshop software for separation of the RGB channels and selection of the specific regions. These regions of interest (ROI) were chosen from each image for intensity and feature analysis in order to find a metric which would allow discrimination of different tissue types. The ROI from colposcopic images with neoplasia and immature squamous metaplasia were chosen specifically to correspond to the biopsy sites, while areas of mature squamous epithelium were chosen from arbitrary representative sites of the image.

#### 2.3.1 RGB Values

The most obvious choice of parameters to examine in a color image are the raw red, green, and blue (RGB) pixel intensity values within the regions of interest. Interpatient variability combined with the automatic gain of most imaging systems make the absolute intensity an unreliable parameter to use, so that here the relative contribution of R, B, and G are examined, which can also be called the chromaticity coordinate [i.e.,  $R/(R+B+G)$  is the relative red pixel intensity as a fraction of 1]. Images were analyzed with Adobe Photoshop software to separate RGB images of the ROI, and to count absolute RGB values along with standard deviations.

#### 2.3.2 RGB Variations

Since variation of the intensity was observed significantly in all regions of interest, this was tracked for each site. The variation in the intensity was calculated as the standard deviation of the intensity divided by the absolute intensity of the region, for RGB values separately. This provided a relative variation measure over the region of interest. In this analysis, care was taken to make sure that the area of the region of interest was roughly the same, so that the sample size was sufficient to minimize the error due to random fluctuations to less than 1% (i.e., a minimum of 10 000 pixels in each ROI image).

#### 2.3.3 Radial Frequency Analysis-Zeroth Frequency Amplitude

One of the easiest methods to examine patterns in an image is to use the two-dimensional (2D) fast Fourier transform (FFT) algorithm to provide quantitative numbers for the amplitude of different spatial frequencies which compose an image. For this Fourier analysis care was taken to ensure that the magnification of each image was similar ( $16 \times$ ) to ensure that the effect of pixel size did not distort the results. The regions of interest were chosen to coincide with the biopsy results for the CIN 2/3 and the immature squamous metaplasia. The regions were cropped to  $96 \times 96$  pixels to increase the allowed use of the FFT, rather than the slower full Fourier transform algorithm. All calculations were performed in MATLAB using the separated images from the red, green, and blue channels of the RGB image. The resulting transformed image data was reor-

ganized so that the zeroth frequency was at the center of the image, and the 2D data was converted to a one-dimensional array of data by summing spatial frequencies radially around the central (zeroth) frequency.<sup>11</sup> The amplitudes at each spatial frequency were then displayed as logarithmic data. In order to quantitatively compare the spatial frequency features of the images, two particular frequency regions were examined. First the zeroth spatial frequency relative to the next following frequency was calculated for all three red, green, and blue channels of each image, which is the difference in logarithmic values between the zeroth and first spatial frequency amplitudes. This measure of the difference between zeroth and first frequencies is a metric of the amount of the image which is homogeneous (i.e., no changes in intensity).

#### 2.3.4 Radial Frequency Analysis-Slope of Logarithmic Frequency Amplitude

The second analysis was carried out by calculating the slope of the logarithm of spatial frequency amplitude as a function of spatial frequency. This slope was calculated within the frequency range between the 5<sup>th</sup> and the 25<sup>th</sup> spatial frequencies, where the slope of log amplitude versus frequency was linear in most cases. This slope is a measure of how complicated the image is, since more complex images tend to have a higher slope in this range of frequencies. In essence this number is related to the fractal dimension of the image, since it is a measure of the increasing complexity contained within the image as a function of spatial frequency. However it should be noted that the method to calculate this number is quite different than the next method (following section) so that there is no guarantee that the two numbers will agree.

#### 2.3.5 Fractal Dimension

In an effort to describe the complexity of each image, the fractal number of each ROI was calculated. The methodology for this is described in Refs. 12 and 13 where a box counting method was detailed. The box counting method works for binary images (black and white only with no gray scale), so that the ROI in each case was converted from a blue pixel image to a binary image by automating the program to choose the threshold which produced 50% black and 50% white in the image. Initial measurements were also taken with thresholding based upon the best value to preserve the texture of the image, however the former algorithm was used to preserve objectivity in the analysis. Briefly, the box counting method uses square box regions translated around the ROI to determine the number of areas where the box is homogenous and all black. Once the number of box areas are counted, then the size of the box is increased, and the process is repeated. The algorithm used here was programmed into MATLAB and the fractal number was calculated using the equation below

$$D_f = \lim_{d \rightarrow 0} [\ln N(d)] / [\ln(1/d)], \quad (1)$$

where  $N(d)$  is the number of squares required to cover the details contained in the thresholded image to be analyzed, where the square has each side of length,  $d$ . For simplicity, the slope of the ratio in Eq. (1) was used as the fractal dimension. If an image has no features, it has fractal dimension  $D_f=0$ , whereas the most complicated structures have  $D_f=3.0$ . In

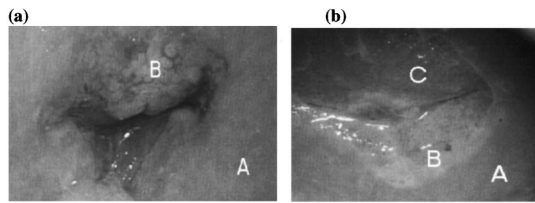


**Fig. 1** (a) Symptomatic cervical image displaying (A) mature squamous epithelium, and (B) CIN 2/3 at the 12 o'clock position. (b) Normal cervical image displaying (A) mature squamous epithelium, (B) acetowhitened immature squamous metaplasia, (C) glandular tissue.

practice, the value of  $d$  was varied over 1.5 orders of magnitude, since fractal patterns need to be analyzed over orders of magnitude for good accuracy.

### 2.3.6 Euler Number

Another measure of the complexity of an image is to count the number of arbitrary sized objects present in the image. The MATLAB function to calculate the Euler number of the image was used for this task.<sup>14</sup> The Euler number is defined as the number of objects in the image subtracted by the number of holes in these objects.<sup>15,16</sup> While this number is a measure of the whole image, it is calculated in practice by analyzing the  $2 \times 2$  pixel patterns across the image systematically for a binary image. The procedure used for analysis of ROI was to take the blue pixel map only, and convert it to a binary (black and white image only) by automatically choosing the threshold value which would convert the image to 50% black and 50% white on average. Then the MATLAB subroutine calculated the Euler number from this image using  $2 \times 2$  pixels (or bit quads) for analysis. Three types of pixel patterns are counted across the image: ( $p_1$ ) those with four zeros, ( $p_2$ ) those with three ones and one zero, and ( $p_3$ ) those with two zeros and two ones in a diagonal pattern only. From these three patterns, the Euler number is calculated by

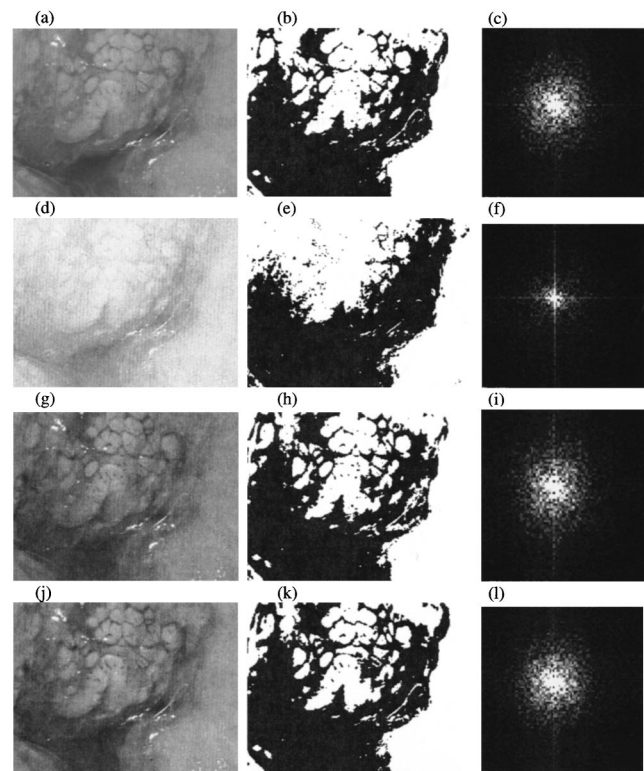
$$E = 1/4[n_{p1} - n_{p2} + 2n_{p3}], \quad (2)$$

where  $n_{p1}$  is the number of  $2 \times 2$  pixel regions with pattern  $p_1$ , and similarly labeled for  $p_2$  and  $p_3$ . Interestingly, this analysis estimates the number of objects in the image minus the number of holes in the objects, but this type of analysis cannot be used to just measure the number of holes or objects alone.<sup>15</sup> In the case of colposcopy images, this number is useful since many of the relevant textures are circular with intricate patterns from blood vessels and glandular regions.

## 3 Results

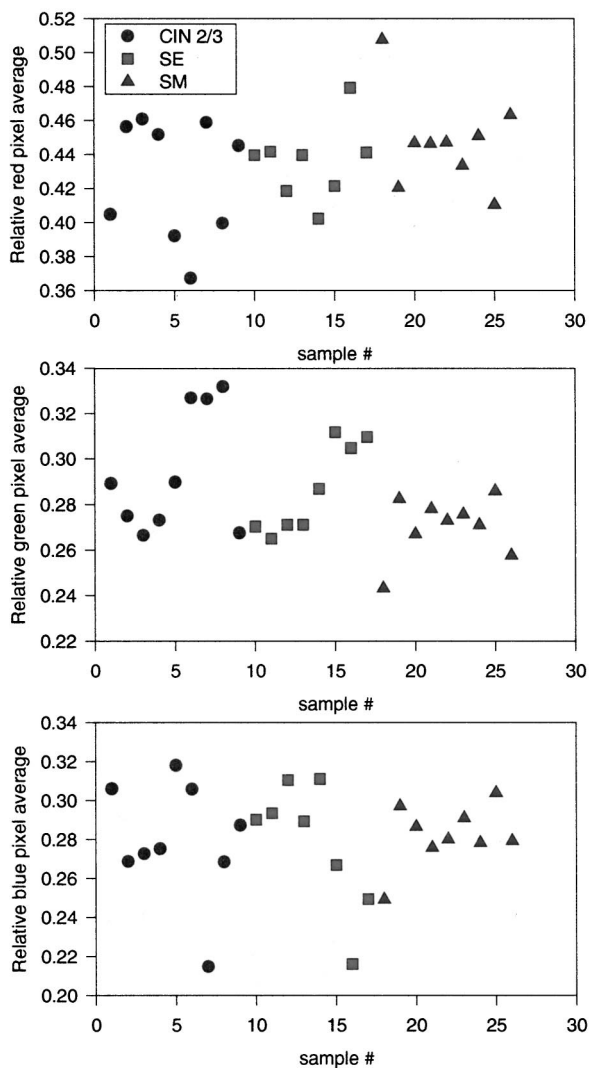
The ROI of CIN 2/3 in the diseased cervical images were all chosen to correspond to the biopsy site results so that pathologic confirmation of the disease state was known. The ROI of mature squamous epithelium (MSE) were chosen randomly from the images, within the homogenous tissue areas, and the ROI of immature squamous metaplasia (ISM) were chosen from the biopsy confirmed sites in each image. Table 1 shows the pathologic grade of the nine diseased cervical images used in this study. All samples with immature squamous metaplasia had similar biopsy results.

Figure 1 shows two typical colposcopic images, where the



**Fig. 2** A magnified image of the cervix in Figure 1(a) is shown in full RGB in (a), with just the red channel in (d), just the green channel in (g), and just the blue channel in (j). In the second column (b), (e), (h), (k), the images have been segmented to provide 50% of black and white by thresholding the corresponding image to the left of it. In the third column (c), (f), (i), (l), the gray scale images in column one have been Fourier transformed with a two-dimensional FFT algorithm. The thresholding shown in the second column was used for fractal dimension calculation and Euler number calculation, while the Fourier transformed images in column three were used to calculate the spatial frequency distributions of the images.

first displays a diseased region of CIN 2/3 above the squamo-columnar junction, within the transformation zone; and the second image has only ISM in the same region. While the images from all the patients varied considerably, these two images show one type of difference which is possible in the color and texture patterns of the image. The three categories of tissue chosen for this study are shown in these two images. To compare the features which can be analyzed in a typical image, a closer image of the cervix in Figure 1(a) is shown in Figure 2(a) at  $16 \times$  magnification, and the red, green, and blue fractions of the image were separated and are shown in Figures 2(d), 2(g), and 2(j), respectively. These images are all thresholded using an algorithm which was designed to produce 50% black and 50% white images (binary images). The resulting images from each channel provides unique patterns which are reflective of the tissue optical properties in that particular wavelength range. These patterned images were used for determination of the fractal dimension and the Euler number. Alternatively, the original R, G, and B images can be Fourier transformed to produce 2D plots of the spatial frequency amplitude. In Figure 2, the 3<sup>rd</sup> column (c), (f), (i), and (l) shows the result of performing a 2D FFT of the central  $128 \times 128$  region of pixels from each image (a), (d), (g), and



**Fig. 3** Relative average intensity values as calculated for the region of interest for each colposcope image sample, with the three graphs displaying data for red pixel values in the top graph, green pixel values in the middle graph, and blue pixel values in the bottom graph. All numbers are the average of at least 10<sup>4</sup> pixels in an ROI.

(j), respectively. These images are arranged so that the zeroth spatial frequency is at the center of the image, and a radial binning around this central location provides a linear array of amplitudes at increasing spatial frequency.

The ROI analysis for relative red, green, and blue values (also called the chromaticity coordinate) are shown in Figures 3(a)–3(c), respectively. The data are plotted as sample number in order to show all samples and the variance in the data points. The unpaired students T test was used to determine if there was a statistically significant separation of the data between different tissue types for all three RGB values. No comparisons between any of the tissue types for any of the three RGB values produced probability values of less than 0.1, indicating that individual colors of the tissues were not sufficient to discriminate between types.

The variation in the RGB values was examined in the same manner, for the same ROI areas. Graphs of the data for red, green, and blue are shown in Figures 4(a)–4(c), respectively.

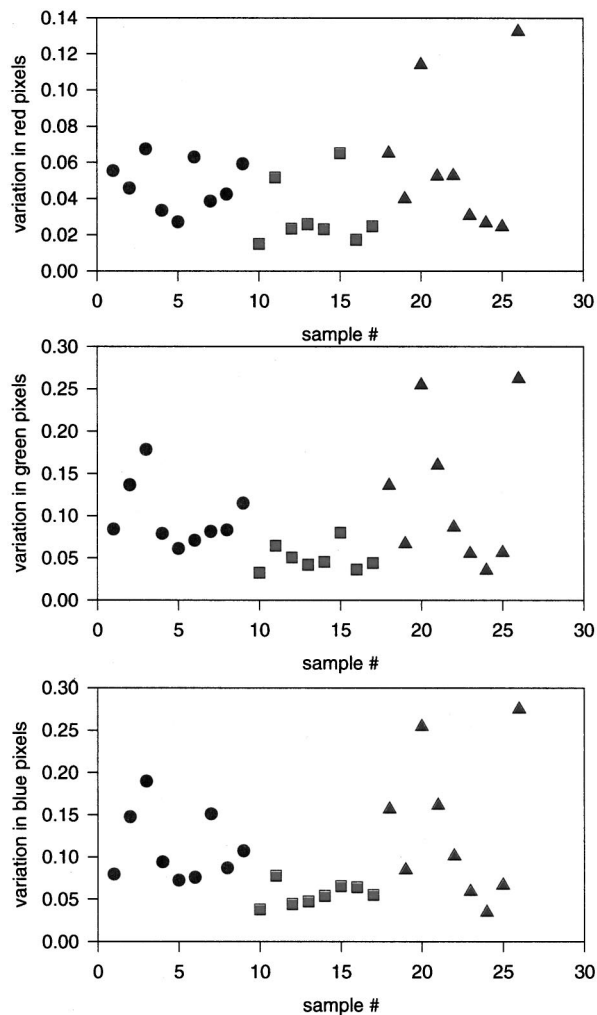


**Fig. 4** Intensity variations calculated as the standard deviation of the pixel values divided by the average pixel value. Graphs are (top graph) red pixels, (middle graph) green pixels, and (bottom graph) blue pixels.

In this case the ability to discriminate between tissue types was improved, based on the students T test. The *P* values for the three different tissue types and three color variations are shown in Table 2. The results indicate that the variation in the RGB values are a reliable method for separating CIN 2/3 or

**Table 2** Calculated probabilities that the data sets do not have different mean values, using an unpaired students T test. (*P* < 0.05 is considered statistically significant separation of data sets). Abbreviations are CIN=cervical intraepithelial neoplasia, ISM=immature squamous metaplasia, MSE=mature squamous epithelium, and statistically significant differences are denoted with an asterisk (\*).

Data sets compared	<i>P</i> value (R st. dev.)	<i>P</i> value (G st. dev.)	<i>P</i> value (B st. dev.)
CIN vs MSE	0.048	0.004*	0.002*
CIN vs ISM	0.4	0.44	0.51
ISM vs MSE	0.07	0.03*	0.03*

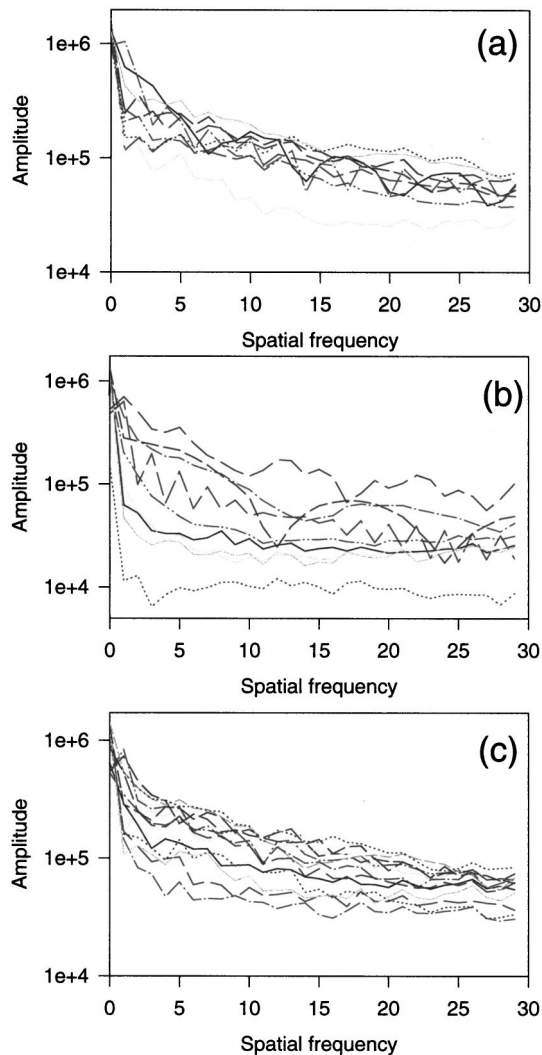


**Fig. 5** Plots of the amplitude of the spatial frequency distribution from the two-dimensional Fourier transform of the regions of interest in each image for (a) CIN 2/3, (b) mature squamous epithelium, and (c) immature squamous metaplasia. The spatial frequency amplitude was calculated by radially adding frequencies around the central (zeroth) frequency bin (as can be observed in the images of the 3rd column of Figure 2).

ISM from mature squamous epithelium, but that CIN 2/3 and ISM cannot be reliably separated from each other in this manner. Interestingly, the green and blue channels provide the best separation between tissues. Qualitatively the green channel appears to emphasize blood vessel and glandular locations, whereas the blue channel improves the resolution of epithelial tissue layers and patterns.

The radial spatial frequency analysis was carried out for all image ROIs for each of the R, G, and B channels separately. The typical results from a radial binning of the spatial frequencies is shown in Figure 5(a) for mature squamous epithelium, 5(b) for CIN 2/3, and 5(c) for ISM. The shapes of these curves indicates that there is a pronounced peak at the zeroth spatial frequency for all images, as expected, and that the CIN and SM data generally has a higher gradient in the amplitude with increasing spatial frequency. The data is displayed as logarithm of frequency amplitude versus spatial frequency

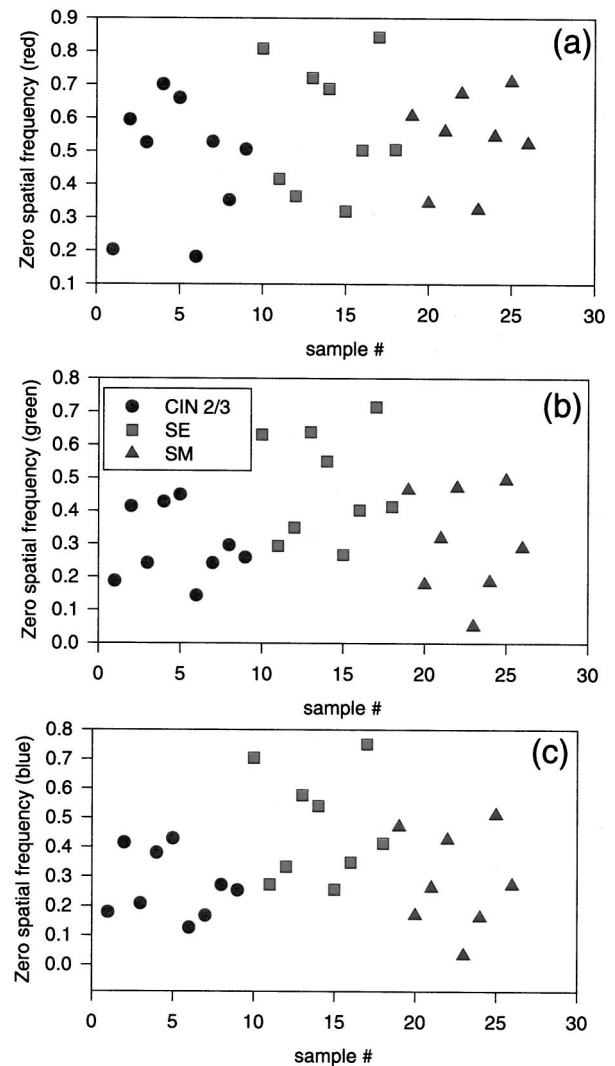


**Fig. 6** Calculation of the amplitude of the logarithm of the zeroth spatial frequency relative to the next higher frequency for each of the Fourier transformed regions of interest, showing results from (a) the red channel, (b) the green channel, and (c) the blue channel. The typical changes between the zeroth frequency and the next highest frequency can be seen in the plots of Figure 4.

number, in Figure 5. The peak value from these graphs at the zeroth frequency was calculated relative to the first spatial frequency amplitude, providing a measure of the difference in log values between the zeroth and first spatial frequency amplitudes. This calculation was carried out for all images and for all R, G, and B channels, the results are plotted in Figure 6. An unpaired students T test was used to compare the discrimination of the calculated data, and the *P* values from this comparison are shown in Table 3. This zeroth to first frequency amplitude difference could be used to discriminate between CIN 2/3 and MSE or between ISM and MSE using either the green or the blue images, but not the red image.

While the zeroth spatial frequency is related to the homogeneous regions of the image, the higher spatial frequencies (above zero) are related to the more complex features of the images. Based upon the data in Figure 5, it was hypothesized that the slope of the  $\log(\text{amplitude})$  versus spatial frequency

**Table 3** Calculated probabilities that the data sets do not have different mean values, using an unpaired students T test to compare the data of the amplitude of the zeroth frequency bin from the FFT of each ROI, as plotted in Figure 6. Abbreviations are as in Table 2, and statistically significant differences are denoted with an asterisk (\*).

Data sets compared	<i>P</i> value ( <i>R</i> zero freq.)	<i>P</i> value ( <i>G</i> zero freq.)	<i>P</i> value ( <i>B</i> zero freq.)
CIN vs MSE	0.27	0.016*	0.015*
CIN vs ISM	0.44	0.87	0.79
ISM vs MSE	0.65	0.052*	0.056*

would be a good indicator of the complexity of the images. The slope of the log(amplitude) versus spatial frequency was calculated for all of the images using red, green, and blue images for all ROI sections, using the frequency range between 5 and 25 (see Figure 5 as a reference). The data from this analysis is plotted in Figure 7, and the results from a students T test comparison is used to calculate probabilities of different distributions (Table 4). Again, the results indicate that this analysis can be used to differentiate between CIN 2/3 and MSE or between ISM and MSE, but not between CIN 2/3 and ISM, using only the blue and green channels.

The fractal dimension was calculated for each tissue type with automatic segmentation of the images. The calculation was carried out on all three R, G, and B channels using binary (black and white) versions of each image which were obtained by thresholding to provide 50% white and 50% black in each image. One set of typical thresholded binary images for the R, G, and B channels separately, is shown in Figure 2, in the third column. The calculated fractal dimension numbers are plotted in Figure 8. Statistical analysis indicated that the fractal number was insufficient to discriminate between any of the tissue types ( $P > 0.05$  for all comparisons), so that a table of values is not provided here.

The Euler number was calculated for each tissue ROI with automatic segmentation of the images, and the data is plotted in Figure 9. Each of the R, G, and B channels were used again for this analysis, as in the fractal dimension, using binary images thresholded in the manner described in Figure 2. The students T-test comparison between the data sets is shown in Table 5. In this case, the Euler number cannot be used to discriminate between CIN 2/3 and MSE or between ISM and MSE. The ability to separate CIN 2/3 and ISM was significant here ( $P = 0.013$ ). A further improvement in separating the data sets is possible with a different level of thresholding used in the images; however it is difficult to objectively determine which level of thresholding provides the best separation between calculated Euler number for differentiating ISM and CIN 2/3. To address this question, thresholding was done at all possible values for all blue channel images, and the Euler number was calculated as a function of the fraction of the image which appeared white (ranging between 0% and 100%). The results for this analysis for all CIN 2/3 tissue samples are shown in Figure 10(a) and for all ISM tissue samples are shown in Figure 10(b). A comparison of the data in the two graphs indicates that there is maximal deviation

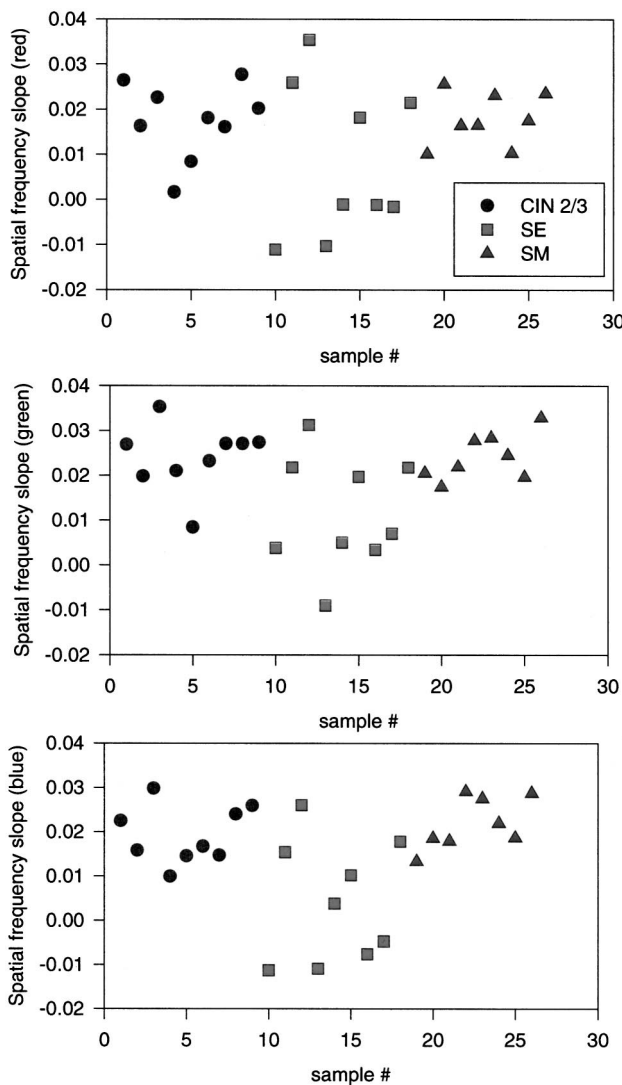


**Fig. 7** Plots of the calculated slope of the logarithm of the spatial frequency amplitude with frequency for all three channels (a) red, (b) green, and (c) blue. The slope was calculated between the 5th and 25th frequency channels on plots as shown in Figure 4, using linear regression.

**Table 4** Calculated probabilities that the data sets do not have different mean values, using an unpaired students T test to compare the data of the slope of the log amplitude of the spatial frequencies, as plotted in Figure 7. Abbreviations are as in Table 2, and statistically significant differences are denoted with an asterisk (\*).

Data sets compared	<i>P</i> value ( <i>R</i> freq. slope)	<i>P</i> value ( <i>G</i> freq. slope)	<i>P</i> value ( <i>B</i> freq. slope)
CIN vs MSE	0.17	0.022*	0.009*
CIN vs ISM	0.91	0.97	0.40
ISM vs MSE	0.16	0.020*	0.004*

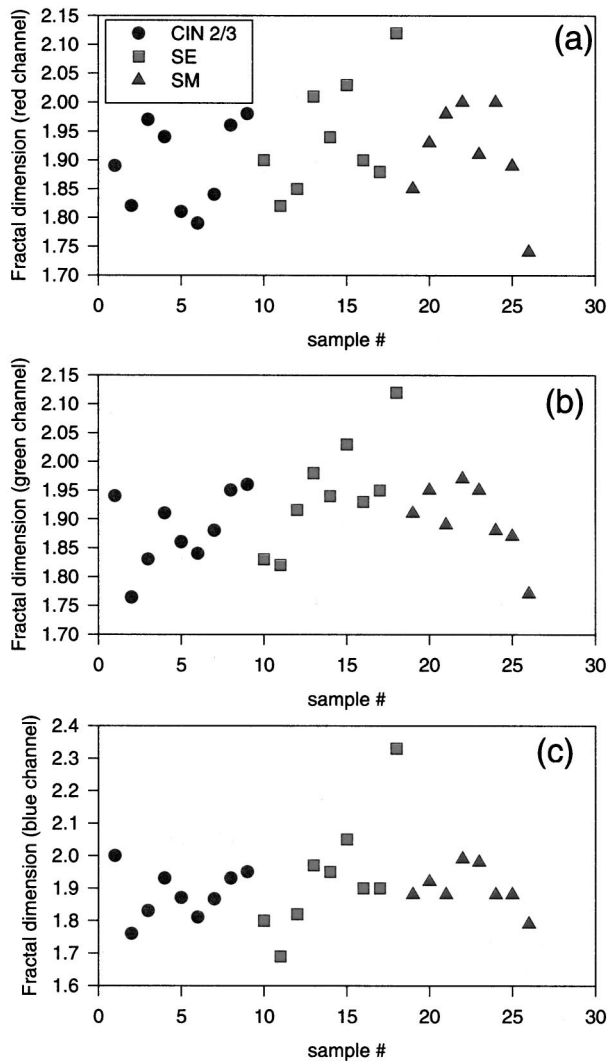


**Fig. 8** Calculated fractal dimension plotted for all the tissue samples using the region of interest chosen and thresholded to provide 50% white and 50% black binary images, using the data from (a) the red channel, (b) the green channel, and (c) the blue channel. The typical appearance of the images after thresholding can be seen in the 3rd column of Figure 2. The box counting method was used to calculate fractal dimension, as described in the text.

between the two sets of values between threshold values of approximately 0.2 to 0.5.

#### 4 Discussion

The main goal of this study has been to determine the pertinent color features in digital colposcopy images which can be used for semiautomated discrimination of different tissue types and malignancies. While it is unlikely that feature analysis can replace expert physician inspection of images, there is a role for feature analysis in objectively quantifying the color changes and structural changes of certain regions of the image. This type of analysis can be important in several roles such as: (i) training new colposcopists, (ii) confirmation of the colposcopic impression, (iii) aiding providers in remote regions to make colposcopic impressions by telecolposcopy, (iv) providing quantitative classification of the color and fea-

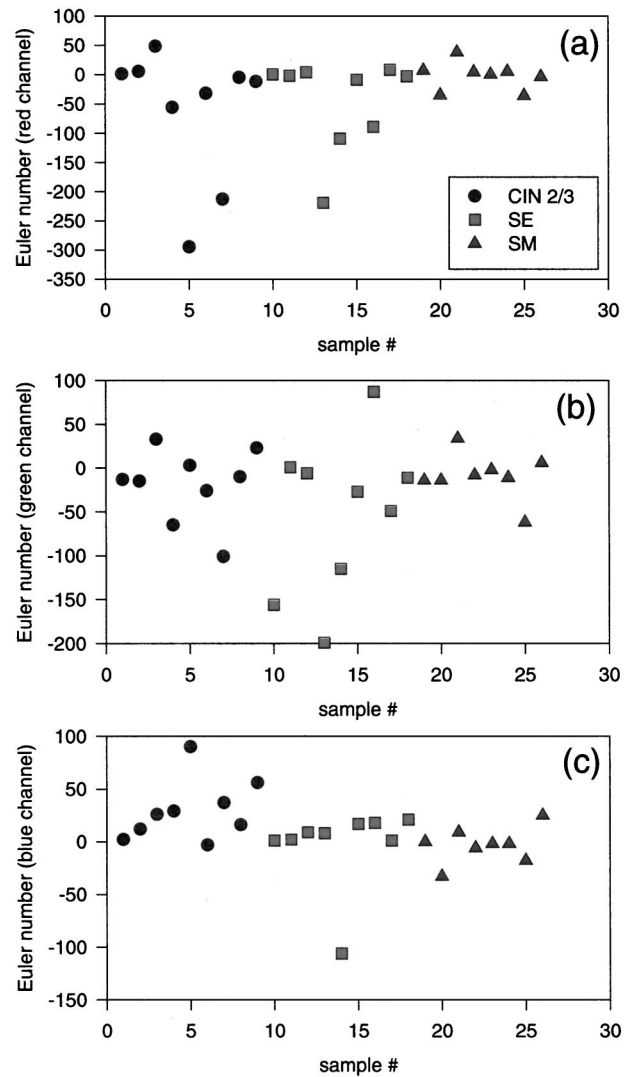


**Fig. 9** Calculated Euler number for all of the image regions of interest using (a) the red channel, (b) the green channel, and (c) the blue channel. The Euler number was calculated from the thresholded binary images as shown in the 3rd column of Figure 2, and is defined as the number of black objects minus the number of white holes within the black objects.

**Table 5** Calculated probabilities that the data sets do not have different mean values, using an unpaired students T test to compare the data of Euler number, as plotted in Figure 8. Abbreviations are as in Table 2, and statistically significant differences are denoted with an asterisk (\*).

Data sets compared	<i>P</i> value (R Euler No.)	<i>P</i> value (G Euler No.)	<i>P</i> value (B Euler No.)
CIN vs MSE	0.74	0.32	0.062
CIN vs ISM	0.17	0.56	0.013*
ISM vs MSE	0.15	0.20	0.99

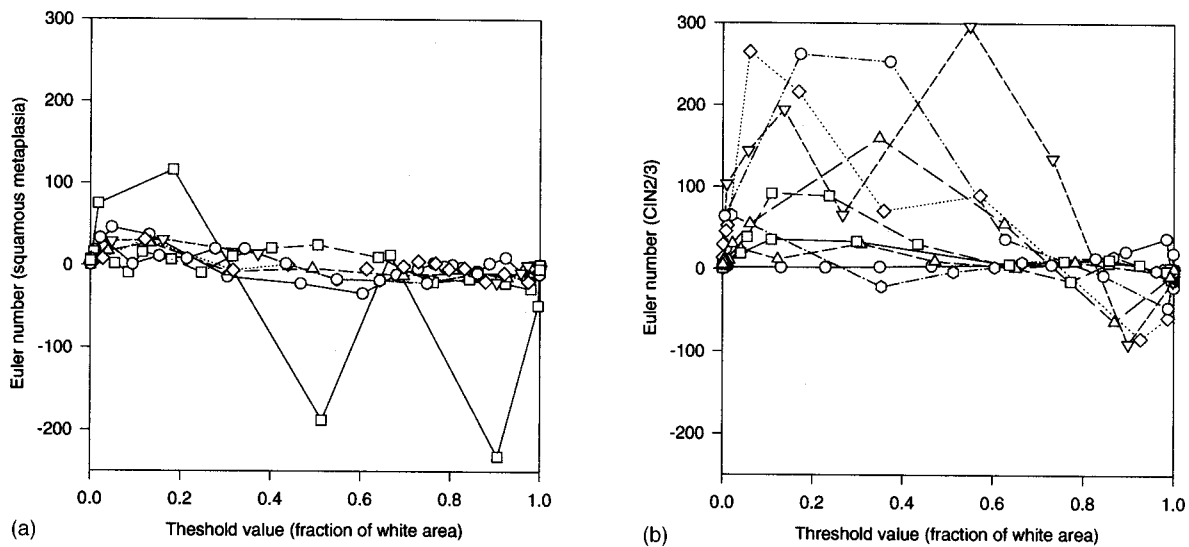


**Fig. 10** (a) Calculated Euler number for the immature squamous metaplasia ROI samples as a function of the level of thresholding in the image, for blue channel images only. (b) Calculated Euler number for the CIN 2/3 ROI samples as a function of threshold value, for the blue channel only. A comparison of the two graphs indicates that maximal difference between the two graphs would be between threshold values of 0.2–0.5.

tures associated with malignant changes in the cervix, and (v) potentially enhancement of the pertinent clinical features through online image preprocessing. The type of color analyses completed here are similar to endoscopy studies which have shown promise in diagnosing colon polyps based upon color changes in the RGB values from video images.<sup>11</sup> Similarly the feature analysis here using fractal dimension is based upon other studies which showed that these can be representative of malignancy based upon the complexity of the blood vessel patterns developed.<sup>11–13</sup> Enhancement of the pertinent features of an image has also been demonstrated in endoscopy by Nishioka and Mycek.<sup>17</sup>

In epithelial tissues, many diseases are characterized by abnormalities having different blood volume content than normal mucosa. In the visible region of the electromagnetic spectrum, hemoglobin in the blood is the major chromophore in soft tissues, with two broad absorption bands in the visible spectrum roughly corresponding to the wavelengths of “blue” and “green” colors of light.<sup>18</sup> Therefore, when the cervix is viewed under white light during endoscopy, the hemoglobin underlying the epithelial cell layers absorbs most of the incident blue light and green light, while scattering most of the incident red light back to the camera. For this reason, the cervix looks generally pinkish-red in color and variations in the local blood vessel density or epithelial cell layer thickness appear as changes in color relative to normal tissue. Thus, glandular epithelium, which has only one layer of columnar epithelium overlying its vasculature usually appears “redder” than normal tissue. The islands of epithelial tissue which are white upon the background of glandular and vascular tissue provide the patterns which can be interpreted with metrics such as the fractal dimension or the Euler number.

A study of the RGB color patterns in the three different tissue types studied here disappointingly indicates that discrimination of immature squamous metaplasia from CIN 2/3 is difficult, and likely impossible, simply based upon the relative RGB values or even upon the variance in these values.

This finding is perhaps not surprising considering that the diagnosis of CIN 2/3 is based on a constellation of visual clues that can be extremely different from patient to patient. However, some fundamental insight about these different tissues can be gleaned from these comparisons, in that the RGB channels of the images yield distinctly different information about the tissue layers. For example, the blue light image discriminates surface cell tissue layers and also provides good contrast between epithelial tissue and blood vessels, while green light discriminates blood vessels very well from all other tissues, and red light provides much less contrast between blood and tissues. Based upon these observations, we hypothesized that the blue light channel of the images would provide the best discrimination between CIN 2/3 and immature squamous metaplasia. The ability to discriminate between features within the transition zone and the mature squamous epithelium may appear trivial to the experienced colposcopist, however achieving this in a robust automated manner with image processing is not always as trivial. Therefore the analysis in Figure 3, and Table 2 indicates that the variance in either the green or blue channels over a region can be used to segment these two different tissue types. Since this is such an easy feature to calculate, it can be a reliable and robust method for future use.

The fractal dimension is an obvious choice of a feature which is well understood in image processing, and has definitively been shown to be a reliable indicator of blood vessel pattern complexity.<sup>12,13</sup> In this analysis, the fractal pattern was not a useful method to discriminate between tissue types, mainly due to the problems of automated thresholding of the images. The fractal analysis requires that RGB images be turned into thresholded binary images before the box counting method can be applied. In our case, to be as objective as possible, the thresholding was done with each image producing 50% black pixels and 50% white pixels automatically. In these images, variations in the light intensity produced complexity patterns even in the squamous epithelium regions of

the image. Thus light variations across the image can confound the feature analysis of fractal dimension, making this a less reliable metric to discriminate between tissues. This problem is clearly an artifact which can be eliminated in future work either through careful analysis of tissues which are only in a certain field of the image, or through the use of online image enhancing processors.<sup>17</sup> One improvement to our thresholding would be to use more sophisticated methods of threshold choice, such as Max-Lloyd quantization, which is used to separate the histogram of gray-scale values into two regions, and the threshold is chosen at the minimum between these two regions. This latter method could provide a more robust method for choosing the threshold level, assuming that the images are all bilobal in histogram gray-scale values.

Fractal dimension calculated by the box counting method may also be related to the calculation of spatial frequency slope, as calculated from the Fourier transformed data. However there does not necessarily have to be a direct relation here since the former was calculated on thresholded images whereas the FFT was completed on gray-scale images. While neither of these two methods provided a clinically useful method of separating CIN 2/3 regions from squamous metaplasia, further exploration of the relative differences between these two methods may elucidate which is the more robust measure of fractal dimension calculation. It is still controversial whether angiogenesis is a good predictive indicator of cervical intraepithelial neoplasia<sup>19</sup> so that at this time it is not obvious if the fractal dimension as calculated from the vascular pattern would be a good predictor. However in other tumor sites there is clear evidence of angiogenesis marking carcinoma, so further investigation of this fractal number seems warranted. Perhaps the most confounding problem for this analysis is that the potential fractal pattern of the vasculature is overlaid with larger regions of epithelial tissue, thus potentially obscuring the blood vessel pattern.

The feature analysis obtained with the calculation of the Euler number appears more promising for a metric which is able to discriminate between all three tissue types compared here. The separation of mature squamous epithelium from CIN 2/3 or immature squamous metaplasia could be achieved with this metric. The discrimination of CIN 2/3 from immature squamous metaplasia was not statistically significant ( $P = 0.08$ ) but is potentially an indicator that this can be a first order method to categorize the complexity of the image. It is not realistic to expect that an automated feature extraction algorithm can always separate CIN 2/3 from immature squamous metaplasia, especially since this cannot always be done by the experienced colposcopist unless biopsy confirmation is used. The eventual goal of this work is to provide some objective metric which discriminates between immature squamous metaplasia, CIN 1 and CIN 2/3 with at least equal to or better specificity than standard colposcopy. This will be tested in further work involving a larger cohort of patient images, and confining the feature analyses used to those which have shown the most promise in this study.

## 5 Conclusions

The most important result of this study is that a feature analysis based method can distinguish between images from patients with CIN 2/3 versus images from patients with imma-

ture squamous metaplasia. In this analysis, comparisons were made with images of squamous epithelium as well simply to provide a tissue type with much simpler features. While many of the methods tested were able to distinguish between SE and SM or SE and CIN 2/3, these are not useful methods for clinical use. The calculation of Euler number was the only statistically significant way to differentiate between CIN 2/3 and SM. The CIN 2/3 images had a higher Euler number than the SM images, as measured from the blue image only. The Euler number is a measure of the number of objects in the image, minus the number of holes in those objects. Therefore the CIN 2/3 images had a higher number of surface tissue objects on a background of darker blood tissue, for the samples used here. Further study of this feature analysis is needed on a larger image data base to determine the sensitivity and specificity of this method.

## Acknowledgments

The authors B.W.P. and D.H. would like to gratefully acknowledge funding from the American Cancer Society Internal Grant Program at the Norris Cotton Cancer Center, and B.W.P. would like to acknowledge partial funding from NCI Contract No. ROICA78734.

## References

1. H. Hinselmann, *Einführung in die Kolposkopie*, Paul Hartung, Hamburg (1933).
2. T. J. Helmerhorst, G. H. Kijkhuizen, J. J. Calame, H. J. Kwikel, and J. G. Stolk, "The accuracy of colposcopically directed biopsy in diagnosis of CIN 2/3," *Eur. J. Obstet. Gyn. Reprod. Biol.* **24**, 221–229 (1987).
3. A. Cinel, M. Oselladore, E. Insacco, and D. Minucci, "The accuracy of colposcopically directed biopsy in the diagnosis of cervical intraepithelial neoplasia," *Eur. J. Gynaecol. Oncol.* **11**, 433–437 (1990).
4. D. G. Ferris, J. T. Cox, L. Burke, M. S. Litaker, D. M. Harper, M. J. Campion, M. D. Greenberg, L. M. Wun, and L. McShane, "Colposcopy quality control: Establishing colposcopy criterion standards for the NCI ALTS trial," *J. Lower Gen. Tract. Dis.* **2**, 195–203 (1998).
5. M. R. Toglia, K. M. Coburn, and M. L. Pearl, "Evaluation of colposcopic skills in an obstetrics and gynecology residency training program," *J. Lower Gen. Tract. Dis.* **1**, 5–8 (1997).
6. M. S. Mikhail, A. Anyaegbunam, and S. L. Romney, "Computerized colposcopy and conservative management of cervical intraepithelial neoplasia in pregnancy," *Acta Obstet. Gynecol. Scand.* **74**, 376–378 (1995).
7. W. E. Crisp, B. L. Craine, and E. A. Craine, "The computerized digital imaging colposcope: Future directions," *Am J. Obstet. Gynecol.* **162**, 1491–1497 (1990).
8. M. I. Shafi and D. M. Luesley, "Modern image capture and data collection technology," *Clin. Obstet. Gynecol.* **38**, 640–643 (1995).
9. A. Szarewski, M. J. Jarvis, P. Sasieni, M. Anderson, R. Edwards, S. J. Steele, J. Guillebaud, and J. Cuzick, "Effect of smoking cessation on cervical lesions size," *Lancet* **347**, 941–943 (1996).
10. P. M. Cristoforoni, D. Gerbaldo, A. Perino, R. Piccoli, F. J. Montz, and G. L. Captiano, "Computerized colposcopy: Results of a pilot study and analysis of its clinical relevance," *Obstet. Gynecol.* **85**, 1011–1016 (1995).
11. M. J. Emerson, "A method to analyze the malignant potential of colorectal polyps using endoscopic images," in *Electronic Engineering*, Massachusetts Institute of Technology, Cambridge (1998).
12. J. W. Baish, Y. Gaxit, D. A. Berk, M. Nozue, L. T. Baxter, and R. K. Jain, "Role of tumor vasculature architecture in nutrient and drug delivery: An invasion percolation-based network approach," *Microvasc. Res.* **51**, 327–346 (1996).

13. L. M. Kirchner, S. P. Schmidt, and B. S. Gruber, "Quantitation of angiogenesis in the chick chorioallantoic membrane model using fractal analysis," *Microvasc. Res.* **51**, 2–14 (1996).
14. MATLAB, *Image Processing Toolbox*, 2nd ed., Users Guide, The Mathworks, Inc., Natick, MA (1997), pp. 11–18.
15. B. Horn, *Robot Vision*, MIT EE & CS Series, MIT Press, Cambridge (1986), pp. 73–77.
16. W. K. Pratt, *Digital Image Processing*, 2nd ed., Wiley, New York (1991), pp. 633–634.
17. N. S. Nishioka and M. A. Mycek, "Initial experience with a real-time video processor for enhancing endoscopic image contrast," *Gastro. Endos.* **48**, 62–66 (1998).
18. B. C. Wilson, M. S. Patterson, S. T. Flock, and J. D. Moulton, *The optical absorption and scattering properties of tissues in the visible and near-infrared wavelength range*, in *Light in Biology and Medicine*, edited by M. Douglas, Dall'Acqua, Plenum, New York (1988), pp. 45–52.
19. O. Abulafia, W. E. Triest, and D. M. Sherer, "Angiogenesis in malignancies of the female genital tract," *Gyne. Oncol.* **72**(2), 220–31 (1999).